Hyperspectral Image Denoising Employing a Spectral–Spatial Adaptive Total Variation Model

Qiangqiang Yuan, Liangpei Zhang, *Senior Member, IEEE*, and Huanfeng Shen, *Member, IEEE*

***Abstract*—The amount of noise included in a hyperspectral image limits its application and has a negative impact on hyperspectral image classification, unmixing, target detection, and so on. In hyperspectral images, because the noise intensity in different bands is different, to better suppress the noise in the high-noise-intensity bands and preserve the detailed information in the low-noise-intensity bands, the denoising strength should be adaptively adjusted with the noise intensity in the different bands. Meanwhile, in the same band, there exist different spatial property regions, such as homogeneous regions and edge or texture regions; to better reduce the noise in the homogeneous regions and preserve the edge and texture information, the denoising strength applied to pixels in different spatial property regions should also be different. Therefore, in this paper, we propose a hyperspectral image denoising algorithm employing a spectral–spatial adaptive total variation (TV) model, in which the spectral noise differences and spatial information differences are both considered in the process of noise reduction. To reduce the computational load in the denoising process, the split Bregman iteration algorithm is employed to optimize the spectral–spatial hyperspectral TV model and accelerate the speed of hyperspectral image denoising. A number of experiments illustrate that the proposed approach can satisfactorily realize the spectral–spatial adaptive mechanism in the denoising process, and superior denoising results are produced.**

***Index Terms*—Hyperspectral image denoising, spatial adaptive, spectral adaptive, split Bregman iteration.**

I. Introduction

OVER the past decades, hyperspectral image (HIS) analysis has matured into one of the most powerful and fastest growing technologies in the field of remote sensing. The hyperspectral data provide contiguous or noncontiguous 10-nm bands throughout the 400–2500-nm region of the electromagnetic spectrum and, hence, have the potential to precisely discriminate different land cover types using the abundant spectral information. Such identification is of great significance for detecting minerals, precision farming, urban planning, etc. [1].

Manuscript received February 22, 2011; revised August 13, 2011 and November 17, 2011; accepted January 8, 2012. Date of publication March 7, 2012; date of current version September 21, 2012. This work was supported in part by the National Basic Research Program of China (973 Program) under Grant 2011CB707103, by the National Natural Science Foundation of China under Grants 40930532, 41071269, 40971220, and 61102128, and by the Program for New Century Excellent Talents by the Ministry of Education (NCET-10-0648).

Q. Yuan and L. Zhang are with the State Key Laboratory of Information Engineering in Surveying, Mapping, and Remote Sensing, Wuhan University, Wuhan 430079, China (e-mail: yqiang86@gmail.com; zlp62@public.wh.hb.cn).

H. Shen is with the School of Resource and Environmental Science, Wuhan University, Wuhan 430079, China (e-mail: shenhf@whu.edu.cn).

Color versions of one or more of the figures in this paper are available online at http://ieeexplore.ieee.org.

Digital Object Identifier 10.1109/TGRS.2012.2185054

Unfortunately, the existence of noise in a hyperspectral image not only influences the visual effect of these images but also limits the precision of the subsequent processing, for example, in classification [2], unmixing [3], subpixel mapping [4], target detection [5], etc. Therefore, it is critical to reduce the noise in the hyperspectral image and improve its quality before the subsequent image interpretation processes.

In recent decades, many hyperspectral image denoising algorithms have been proposed. For example, Atkinson *et al.* [6] proposed a wavelet-based hyperspectral image denoising algorithm, and Othman and Qian [7] proposed a hybrid spatial–spectral derivative-domain wavelet shrinkage noise reduction (HSSNR) approach. The latter algorithm resorts to the spectral derivative domain, where the noise level is elevated, and benefits from the dissimilarity of the signal regularity in the spatial and the spectral dimensions of hyperspectral images. Chen and Qian [8], [9] proposed to perform dimension reduction and hyperspectral image denoising using wavelet shrinking and principal component analysis (PCA). Qian and Lévesque [10] evaluated the HSSNR algorithm on unmixing-based hyperspectral image target detection. Recently, Chen *et al.* [11] proposed a new hyperspectral image denoising algorithm by adding a PCA transform before using wavelet shrinkage; first, a PCA transform was implemented on the original hyperspectral image, and then, the low-energy PCA output channel was denoised with wavelet shrinkage denoising processes. Another type of filter-based hyperspectral image denoising algorithm is based on a tensor model, which was proposed by Letexier and Bourennane [12], and has been evaluated in hyperspectral image target detection [13] and classification [14]. Recently, a filter-based hyperspectral image denoising approach using anisotropic diffusion has also been proposed [15]–[17].

As hyperspectral images have dozens or even hundreds of bands, and the noise intensity in each band is different, the denoising strength should be adaptively adjusted with the noise intensity in each band. In another respect, with the improvements in sensor technology, the development and increasing use of images with both high spatial and spectral resolutions have received more attention. Such high spectral and spatial resolution data provide both detailed structural and spectral information [18]. Within the same band, because there is a variety of different spatial property regions, the noise reduction strength should be adaptively adjusted to different spatial property areas. However, to the best of our knowledge, a suitable hyperspectral image denoising algorithm, which considers this spectral–spatial adaptive mechanism, has not yet been proposed.

In recent years, image denoising based on a total variation (TV) model [19] has been attracting more attention, and it

0196-2892/$31.00 © 2012 IEEE

has been proved that the TV algorithm is a very effective and efficient denoising approach because of its effectiveness in preserving edge information. Apart from the image denoising purpose, the TV model has been developed in many other image processing fields, such as superresolution [20], segmentation [21], and decomposition [22]. In [23]–[28], the authors have developed the TV model into a color image restoration problem, and some color TV (CTV) models have also been proposed. In addition, some spatially adaptive TV (SATV) models have been proposed for gray-level image denoising to better deal with the noise suppression and edge preserving problem [29]–[32]. However, although the proposed CTV model and SATV model work well, they have not been used in the hyperspectral image denoising problem. For the CTV model, it is just used to solve the color image denoising problem, and the SATV model is just used on the gray-level image denoising problem. As described earlier, compared with color images, in hyperspectral images, because noise intensity varies in the different bands and the spatial information in each band is abundant, how to deal with the noise intensity difference in the different bands while preserving the abundant spatial information is a very important and challenging problem. Therefore, it is well worthwhile to extend the TV models to hyperspectral images.

In this paper, we propose a spectral–spatial adaptive hyperspectral TV (SSAHTV) denoising algorithm, in which the noise intensity difference between different bands and spatial property differences between different pixels are both considered. The main ideas and contributions of the proposed approach can be summarized as follows.

1) A spatially adaptive multichannel TV model is used on the hyperspectral denoising problem. This model considers the noise differences between different bands and the interband spatial information differences, and the band and spatial adaptive denoising process is automatically realized.
2) A split Bergman iteration algorithm is used to optimize the proposed hyperspectral TV denoising model, in which the optimization of the denoising model is split into two subproblems, which are very easy to optimize, and a fast denoising speed is achieved.
3) From the experimental results with both simulated and real data, it is found that the proposed SSAHTV model produces good denoising results, and it works very well not only on a Gaussian noise distribution but also on striping noise and some other mixed distribution noise. It may well provide a new idea for hyperspectral image destriping and dead pixel inpainting.

The remainder of this paper is organized as follows. In Section II, the degradation model of the hyperspectral image is introduced, and following this, the maximum *a posteriori* (MAP)-based hyperspectral image denoising model is presented. The SSAHTV model is specifically introduced in Section III. In Section IV, the split Bregman iteration is presented in detail. Some experimental results and discussion are presented in Section V, and finally, some conclusions are given in Section VI.

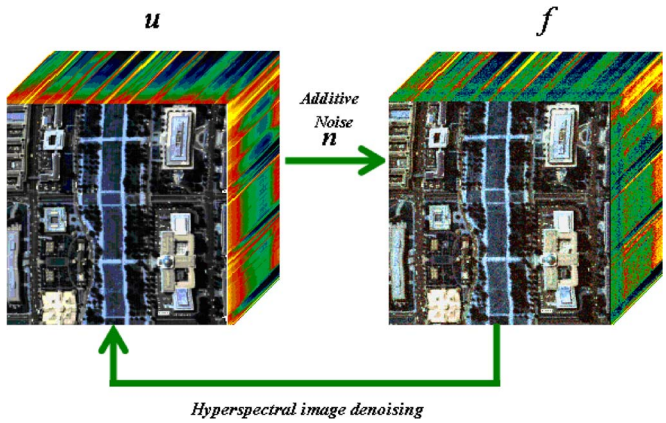

Fig. 1. Noise degradation process of the hyperspectral image.

II. MAP Hyperspectral Image Denoising Model

A. Hyperspectral Noise Degradation Model

Assuming that we have an original hyperspectral image, and the degradation noise is assumed to be additive noise, the noise degradation model of the hyperspectral image can be written as

$$f = u + n \tag{1}$$

where $u = [u_1, u_2, \ldots, u_j \ldots u_B]$ is the original clear hyperspectral image, with the size of $M \times N \times B$, in which M represents the samples of the image, N stands for the lines of the image, and B is the number of bands. $f = [f_1, f_2, \ldots, f_j, \ldots, f_B]$ is the noise degradation image, which is also of size $M \times N \times B$, and $n = [n_1, n_2, \ldots, n_j, \ldots, n_B]$ is the additive noise with the same size as u and f. The degradation process of the hyperspectral image is shown in Fig. 1.

B. MAP Denoising Model

In recent years, the MAP estimation theory, which inherently includes prior constraints in the form of prior probability density functions, has been attracting attention and enjoying increasing popularity. It has been used to solve many image processing problems, which can be formed as ill-posed and inverse problems, such as image denoising [33], destriping and inpainting [34], superresolution reconstruction [35], [36], and others. Therefore, because the hyperspectral image denoising process is an inverse and ill-posed problem, in this paper, the MAP estimation theory is used to solve it.

Based on the MAP estimation theory, the denoising model for a hyperspectral image can be represented as the following constrained least squares problem [34]–[36]:

$$\hat{u} = \arg\min \left\{ \sum_{j=1}^{B} \|u_j - f_j\|_2^2 + \lambda R(u) \right\}. \tag{2}$$

In (2), $\sum_{j=1}^{B} \|u_j - f_j\|_2^2$ is the data fidelity item, which stands for the fidelity between the observed noisy image and the original clear image, and $R(u)$ is the regularization item, which gives a prior model of the original clear hyperspectral image.

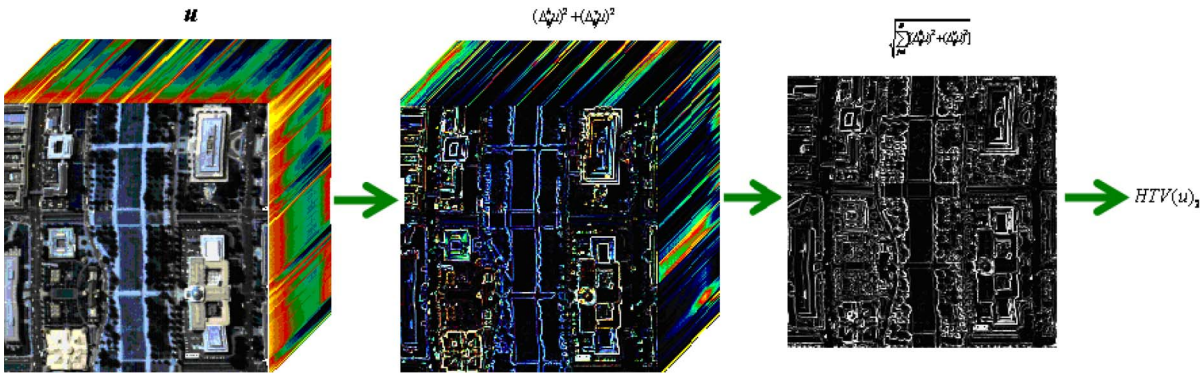

Fig. 2. Formulation process of the hyperspectral TV model in (7).

λ is the regularization parameter, which controls the tradeoff between the data fidelity and regularization item.

III. SSAHTV Model

A. TV Model

The TV model was first proposed by Rudin *et al.* [19] to solve the gray-level image denoising problem because of its property of effectively preserving edge information.

For a gray-level image u, the TV model is defined as follows:

$$TV(u) = \sum_i \sqrt{\left(\nabla_i^h u\right)^2 + \left(\nabla_i^v u\right)^2} \tag{3}$$

where ∇_i^h and ∇_i^v are linear operators corresponding to the horizontal and vertical first-order differences, respectively, at pixel i. $\nabla_i^h u = u_i - u_{r(i)}$ and $\nabla_i^v u = u_i - u_{b(i)}$, where $r(i)$ and $b(i)$ represent the nearest neighbor to the right and below the pixel.

B. Spectral Adaptive Hyperspectral TV Model

The simplest way of extending the TV model to hyperspectral images is by a band-by-band manner, which means that, for every band, the TV model is defined like the gray-level image TV model in (3), and then, the TV model of each band is added together. This simple band-by-band hyperspectral TV model is defined as follows:

$$HTV(u)_1 = \sum_{j=1}^{B} TV(u_j) \tag{4}$$

where u is the hyperspectral image, which has the formation of $u = [u_1, u_2, \ldots, u_j, \ldots, u_B]$, and u_j stands for the jth band of the hyperspectral image.

If we incorporate the band-by-band hyperspectral TV model in (5) into the regularization model in (2), the denoising model can be written as

$$\hat{u} = \arg\min \left\{ \sum_{j=1}^{B} \|u_j - f_j\|_2^2 + \lambda \sum_{j=1}^{B} TV(u_j) \right\} \tag{5}$$

where u_j and f_j are the jth bands of the clear and noisy hyperspectral images, respectively. For (5), the Euler–Lagrange equation is written as [24]

$$(u_j - f_j) - \lambda \nabla \cdot \frac{\nabla u_j}{|\nabla u_j|} = 0. \tag{6}$$

From (6), it means that every band is separately denoised by the single-band TV model, which will cause the following drawback. For a hyperspectral image, because the noise intensity of each band is almost always different, the denoising strength should also be different in each band. However, in (6), if we use the same regularization parameter λ for all the bands, which means that the regularization strength of each band is equal, this arrangement will result in the following: 1) If the high-noise-intensity bands are well denoised using a large λ, the low-noise-intensity bands will be oversmoothed, and 2) conversely, when the low-intensity bands are well denoised using a small λ, the noise in the high-noise-intensity bands will not be well suppressed. Although different λ can be used in different bands to overcome this drawback, manually adjusting the λ in different bands is very time-consuming.

Therefore, how to define a hyperspectral TV model that can adaptively adjust the denoising strength of different bands is a critical problem. To make the denoising process spectrally adaptive, we extend the CTV model proposed in [27] to define the hyperspectral TV model, which has the following formation:

$$HTV(u)_2 = \sum_{i=1}^{MN} \sqrt{\sum_{j=1}^{B} (\nabla_{ij} u)^2} \tag{7}$$

$$(\nabla_{ij} u)^2 = \left(\nabla_{ij}^h u\right)^2 + \left(\nabla_{ij}^v u\right)^2 \tag{8}$$

where MN is the total number of pixels in one hyperspectral band and B is the total number of bands. ∇_{ij}^h and ∇_{ij}^v are linear operators corresponding to the horizontal and vertical first-order differences at the ith pixel in the jth band, respectively. To more clearly explain the formation of the hyperspectral TV model, we use Fig. 2 to illustrate it.

The reason why the hyperspectral TV model defined in (7) can realize the spectral adaptive property in the denoising process can be explained as follows.

If we incorporate the hyperspectral TV model in (7) into (2), it will become

$$\hat{u}=\arg\min\left\{\sum_{j=1}^{B}\|u_j-f_j\|_2^2+\lambda\sum_{i=1}^{MN}\sqrt{\sum_{j=1}^{B}(\nabla_{ij}u)^2}\right\}. \quad (9)$$

In (9), if we take the derivative for u_j, the Euler–Lagrange equation of (9) can be written as [24]

$$(u_j-f_j)-\lambda\nabla\cdot\frac{\nabla u_j}{\sqrt{\sum_{j=1}^{B}(\nabla u_j)^2}}=0. \quad (10)$$

To give a clearer illustration, (10) is written as the following way:

$$(u_j-f_j)-\lambda\nabla\cdot\frac{|\nabla u_j|}{\sqrt{\sum_{j=1}^{B}|\nabla u_j|^2}}\cdot\frac{\nabla u_j}{|\nabla u_j|}=0. \quad (11)$$

Compared with (6), we can see that an adjustment parameter $|\nabla u_j|/\sqrt{\sum_{j=1}^{B}|\nabla u_j|^2}$ is added in (11) to automatically adjust the denoising strength of each band. For the high-noise-intensity bands, as $|\nabla u_j|/\sqrt{\sum_{j=1}^{B}|\nabla u_j|^2}$ has a large value, the denoising strength for these bands will be powerful. Inversely, for the bands with low-intensity noise, as $|\nabla u_j|/\sqrt{\sum_{j=1}^{B}|\nabla u_j|^2}$ has a small value, a weak denoising strength will be used on them.

C. SSAHTV Model

After the spectral adaptive property of the hyperspectral TV model is analyzed, another important problem is how to realize the spatial adaptive aspect in the process of denoising, which means how to adjust the denoising strength in different pixel locations in the same band, with the spatial structure distribution. The spatially adaptive mechanism can be described as follows.

For a hyperspectral image u, we first calculate the gradient information of every band using the following:

$$\nabla u_j=\sqrt{(\nabla^h u_j)^2+(\nabla^v u_j)^2} \quad (12)$$

where $\nabla^h u_j$ and $\nabla^v u_j$ are the horizontal and vertical first-order gradients of u_j and $(\nabla^h u_j)^2$ and $(\nabla^v u_j)^2$ represent the squares of each element of $\nabla^h u_j$ and $\nabla^v u_j$. Next, the gradient information of every band is added together, and the square root is taken of each element of the sum

$$G=\sqrt{\sum_{j=1}^{B}(\nabla u_j)^2}. \quad (13)$$

Let G_i be the ith element of vector G, and a weight parameter W_i, which controls the interband denoising strength, is defined in the following:

$$\tau_i=\frac{1}{1+\mu G_i} \quad (14)$$

$$W_i=\frac{\tau_i}{\overline{\tau}}\overline{\tau}=\frac{\sum_{i=1}^{MN}\tau_i}{MN} \quad (15)$$

where μ is a constant parameter, the range of parameter τ is between [0, 1], and $\overline{\tau}$ is the mean value of τ_i.

To make the process of denoising spatially adaptive, the parameter W_i is added to the hyperspectral TV model in (7), and the SSAHTV model is defined as

$$SSAHTV(u)=\sum_{i=1}^{MN}W_i\sqrt{\sum_{j=1}^{B}(\nabla_{ij}u)^2} \quad (16)$$

where W_i represents the spatial weight of the ith pixel in the hyperspectral TV model.

With the definition in (16), it is clearly seen that, for pixels in smooth regions, the value of the gradient information G_i will be small and the spatial weight W_i will have a high value. Therefore, a powerful denoising strength will be used for these pixels, and the noise in the smooth areas will be suppressed better. Conversely, for the pixels in the edge and texture areas, the value of G_i will be large, and the spatial parameter W_i will have a small value. Thus, a weak denoising strength will be used for them, and the edge and detailed information will be preserved.

With the SSAHTV model, the final MAP denoising model used in this paper can be written as

$$\hat{u}=\arg\min\left\{\sum_{j=1}^{B}\|u_j-f_j\|_2^2+\lambda\sum_{i=1}^{MN}W_i\sqrt{\sum_{j=1}^{B}(\nabla_{ij}u)^2}\right\}. \quad (17)$$

IV. Split Bregman Optimization

A. Split Bregman Optimization

Because of the high-dimension property of hyperspectral images and the nondifference property of the proposed SSAHTV model, how to find an efficient way to optimize the hyperspectral denoising model in (17) is a very challenging problem. Recently, a well-performing optimization method called the split Bregman algorithm was developed by Tom Goldstein and Stanley Osher to solve the L_1 norm-based regularization [37], [38], such as the TV model, etc. They concluded that the split Bregman algorithm could work very efficiently when used to optimize the TV denoising model. Therefore, in this paper, the split Bregman method is extended and used to optimize the SSAHTV denoising model in (17). The basic idea of this optimization algorithm can be stated as follows.

First, an auxiliary variable d is introduced into the optimization process and then added to (17) in the following way:

$$\hat{u}=\arg\min\left\{\|u-f\|_2^2+\lambda\sum_{i=1}^{MN}W_i\sqrt{\sum_{j=1}^{B}(d_{ij})^2}\right\}$$
$$\text{subject to}: d=\nabla u. \quad (18)$$

The constrained problem in (18) can be changed into an unconstrained problem with the Bregman iteration method as follows:

$$\hat{u} = \arg\min \left\{ \|u-f\|_2^2 + \lambda \sum_{i=1}^{MN} W_i \sqrt{\sum_{j=1}^{B} (d_{ij})^2} + \beta \|d - \nabla u - b\|_2^2 \right\}. \quad (19)$$

In (19), the variable b is also an auxiliary one to accelerate the iteration. The minimization of (19) can be performed alternately with the following two subproblems:

$$\text{subproblem } u : \hat{u} = \arg\min \left\{ \|u - f\|_2^2 + \beta \|d - \nabla u - b\|_2^2 \right\} \quad (20)$$

$$\text{subproblem } d : \hat{d} = \arg\min \left\{ \lambda \sum_{i=1}^{MN} W_i \sqrt{\sum_{j=1}^{B} (d_{ij})^2} + \beta \|d - \nabla u - b\|_2^2 \right\}. \quad (21)$$

In the aforementioned equation, to solve the u subproblem, the following equation must be solved:

$$(I - \beta\Delta)u^{k+1} = f + \beta\nabla^T(d - b). \quad (22)$$

For the linear function in (22), because the system is strictly diagonal, one of the most efficient methods uses the Gauss–Seidel iteration algorithm.

The d subproblem equation in (21) can be solved using a shrinkage operator as follows:

$$\begin{aligned} d &= \text{shrink}\left(\sqrt{\sum_{j=1}^{B} (\nabla_{ij} u^{k+1} + b^k)^2}, \frac{\lambda W}{\beta} \right) \\ &= \max\left(0, \sqrt{\sum_{j=1}^{B} (\nabla_{ij} u^{k+1} + b^k)^2} - \frac{\lambda W}{\beta} \right) \\ &\quad \times \frac{\nabla_{ij} u^{k+1} + b}{\sqrt{\sum_{j=1}^{B} (\nabla_{ij} u^{k+1} + b)^2}} \end{aligned} \quad (23)$$

where the shrink operator stands for the soft thresholding method that was proposed in [39]. Finally, for the parameter b, it should be updated in each iteration in the following way:

$$b^{k+1} = b^k + (\nabla u^{k+1} - d^{k+1}). \quad (24)$$

From the earlier introduction, it can be seen that the split Bregman iteration optimization method mainly composites the solution of the two subproblems: the u and d subproblems. The advantage of the split Bregman method is that the difficult optimization problem in (17) is split into the aforementioned two subproblems, which are very easy to optimize. The optimization of the u subproblem is just a fast Gauss–Seidel iteration algorithm, with a linear computational complexity of $O(N^3)$, while the optimization of the d subproblem is just a very efficient soft threshold/shrinkage operator, with a linear computational complexity of $O(N^2)$. That is the reason why the split Bregman algorithm works very efficiently on the proposed SSAHTV denoising model.

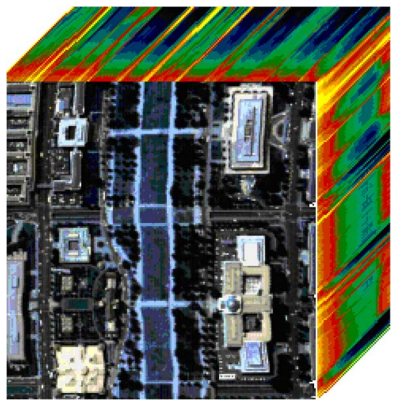

Fig. 3. HYDICE image of Washington DC Mall used in the simulated experiments.

B. Optimization Procedure

Using the split Bregman optimization algorithm, the optimization procedure of the SSAHTV denoising model in (17) can be summarized as follows:

optimization procedure:

Initialize: $u^0 = f$ and $d = 0, b = 0$
  While $\|u^{k+1} - u^k\|_2 \geq tolerance$
  Solve the u subproblem using a Gauss–Seidel iteration algorithm
  Solve the d subproblem using a shrinkage operator as (23)
  Update parameter b: $b^{k+1} = b^k + (\nabla u^{k+1} - d^{k+1})$
End

V. Experimental Results and Discussion

A. Simulated Data Experiments

In the simulated experiments, part of the HYDICE image of Washington DC Mall of a size $200 \times 200 \times 191$ is used to verify the performance of the proposed algorithm. The experimental data in Fig. 3 were provided by Professor David Landgrebe and can be downloaded from [40]. Before the simulated process, the gray values of the hyperspectral image were normalized between [0, 1].

In the simulated process, we simulated the addition of noise in the following two cases.

Case 1) For different bands, the noise intensity is equal: The same distribution of zero-mean Gaussian noise, with a variance of 0.02, is added to all bands. The mean signal-to-noise-ratio (SNR) value is 22.39.

Case 2) For different bands, the noise intensity is different: Different variance zero-mean Gaussian noise is

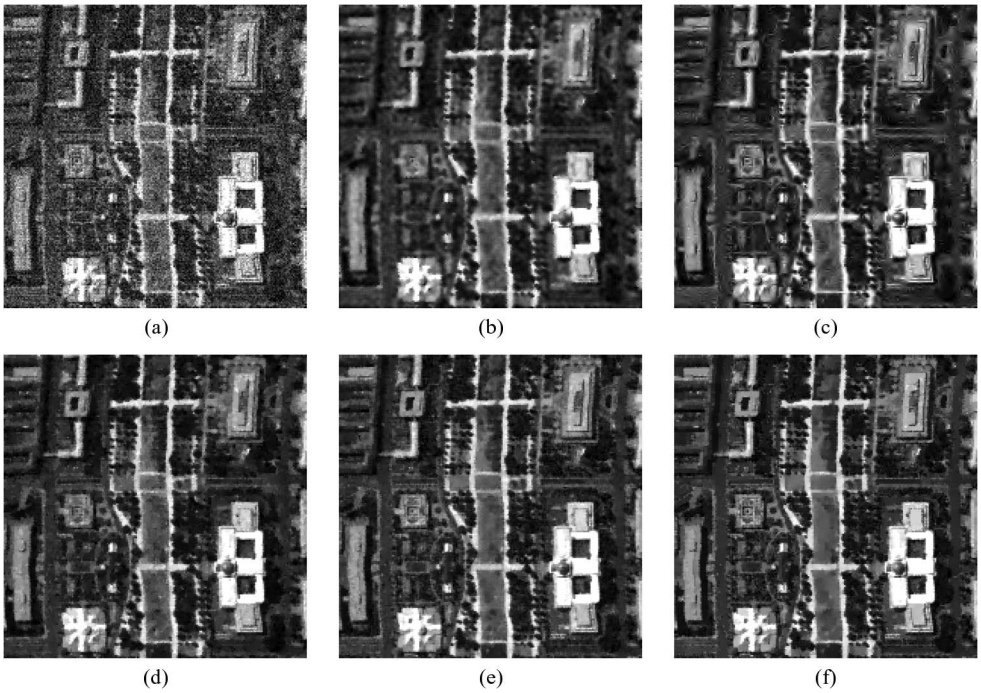

Fig. 4. Denoising results in simulated experiment Case 1. (a) Noise band 191, (b) locally adaptive Wiener, (c) wavelet hard thresholding, (d) band-by-band TV, (e) HTV, and (f) proposed SSAHTV.

added to all bands, with the variance value being randomly selected from 0 to 0.05. The mean SNR value is 22.28.

To verify the performance of the proposed SSAHTV model, it is compared with the locally adaptive Wiener filter (wiener2 function in MATLAB) [41], wavelet hard thresholding denoising [42], the band-by-band TV model in (4), and the hyperspectral TV model in (9).

The peak SNR (PSNR) index is used to give a quantitative assessment of the results of the simulated experiment from the gray-level similarity aspect. Recently, some image quality assessment indices based on the human vision system have been proposed, such as the structural similarity (SSIM) index [43], [44] and the multiscale geometric analysis-based indices [45], [46]. In this paper, we use the SSIM index to give a quantitative assessment of the denoising result from a human vision aspect. For the hyperspectral image, we computed the PSNR and SSIM values between each clear band and denoised band, and then averaged them; they are noted as the mean PSNR (MPSNR) and mean SSIM (MSSIM) indices. The definitions of these evaluation indices are as follows:

$$PSNR = 10\log_{10}\left(\frac{MN}{\|\hat{u}-u\|^2}\right) \tag{25}$$

$$SSIM = \frac{(2\mu_u\mu_{\hat{u}}+C_1)(2\sigma_{u\hat{u}}+C_2)}{(\mu_u^2+\mu_{\hat{u}}^2+C_1)(\sigma_u^2+\sigma_{\hat{u}}^2+C_2)} \tag{26}$$

$$MPSNR = \frac{1}{B}\sum_{j=1}^{B} PSNR_j \tag{27}$$

$$MSSIM = \frac{1}{B}\sum_{j=1}^{B} SSIM_j \tag{28}$$

where MN is the total number of pixels in one band of the hyperspectral image and B is the band number of the hyperspectral image. $\hat{u}$ and u represent the denoised image and the original clear image, and μ_u and $\mu_{\hat{u}}$ represent the average gray values of the original clear and the denoised result, respectively. σ_u and $\sigma_{\hat{u}}$ represent the variances of the original clear image and the denoised image, respectively. $\sigma_{u\hat{u}}$ represents the covariance between the original clear image and the denoised image. C_1 and C_2 are two constants, which prevent unstable results when either $\mu_u^2+\mu_{\hat{u}}^2$ or $\sigma_u^2+\sigma_{\hat{u}}^2$ is very close to zero.

Because there are too many bands in a hyperspectral image, we just select two of them to give a presentation. Figs. 4 and 5 show the denoising results using different methods for bands 191 and 132 in simulated Case 1, and Figs. 7 and 8 show the denoising image using different methods for bands 6 and 108 in simulated Case 2. In Figs. 6 and 9, the PSNR and SSIM values of the different denoising approaches in different bands are presented. The MPSNR and MSSIM of the two cases are presented in Tables I and II, respectively, to give an overall quantitative assessment of the denoising results.

From Figs. 4 and 5 and Figs. 7 and 8, it is shown that the proposed SSAHTV algorithm gives better denoising results, compared to the denoising results of the other four methods. In the SSAHTV denoising result, not only is the noise suppressed more thoroughly but also the edge information and the detailed information are well preserved. However, for the locally adaptive Wiener filter, the denoising result is oversmoothed, and a lot of the detailed information is lost. In the wavelet hard thresholding denoising result, some "artifacts" are produced in the image, and the edge information is also not well preserved. The denoising result using the band-by-band TV model and the hyperspectral TV model is also not as sharp as the denoised

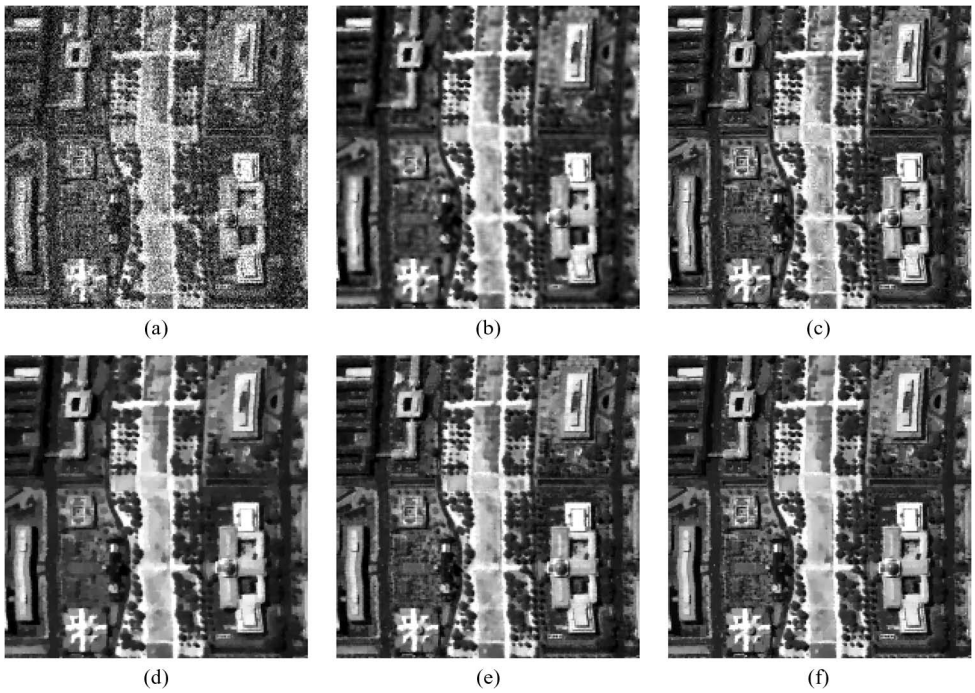

Fig. 5. Denoising results in simulated experiment Case 1. (a) Noise band 132, (b) locally adaptive Wiener, (c) wavelet hard thresholding, (d) band-by-band TV, (e) HTV, and (f) proposed SSAHTV.

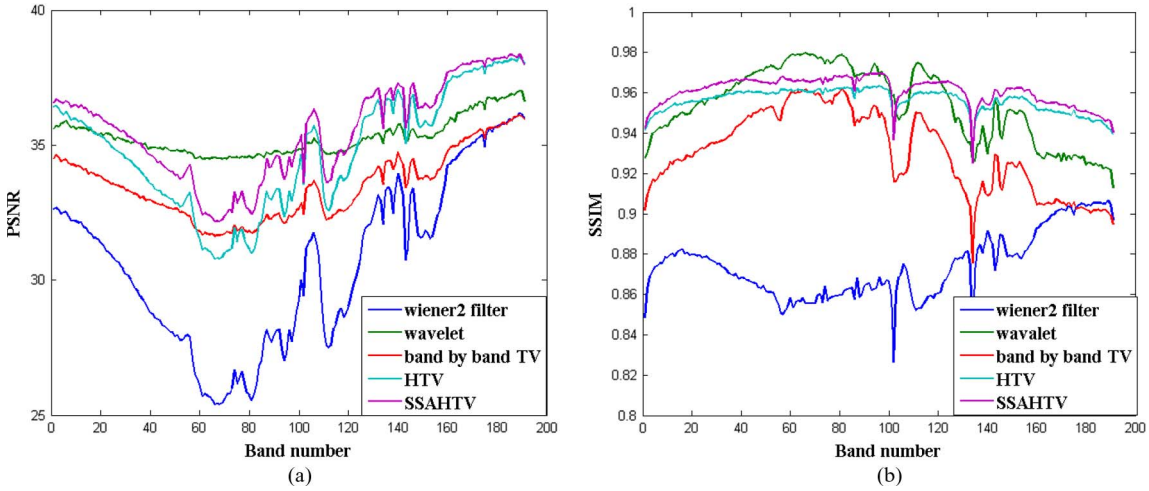

Fig. 6. PSNR and SSIM values of the different denoising approaches in each band of the simulated experiment Case 1. (a) PSNR value. (b) SSIM value.

TABLE I
MPSNR AND MSSIM VALUES OF THE DENOISING RESULTS IN SIMULATED EXPERIMENT CASE 1

	Wiener	Wavelet	Band-by-band TV	HTV	SSAHTV
MPSNR	30.588	35.291	33.488	34.779	35.546
MSSIM	0.87394	0.95395	0.93039	0.95559	0.96061
Time (s)	9.109	164.875	135.061	56.265	52.218

TABLE II
MPSNR AND MSSIM VALUES OF THE DENOISING RESULTS IN SIMULATED EXPERIMENT CASE 2

	Wiener	Wavelet	Band-by-band TV	HTV	SSAHTV
MPSNR	30.132	34.322	33.01	33.839	34.831
MSSIM	0.86306	0.93258	0.91764	0.9374	0.94334
Time (s)	9.188	147.906	309.766	46.172	46.078

image using the proposed SSAHTV model, and some noise still remains in the smooth regions.

The effectiveness of the proposed SSAHTV hyperspectral image denoising algorithm can also be illustrated with the quantitative assessment results shown in Figs. 6 and 9 and Tables I and II. In Figs. 6 and 9, it can be clearly seen that the PSNR and SSIM values of most of the bands using the SSAHTV model are higher than the PSNR and SSIM using

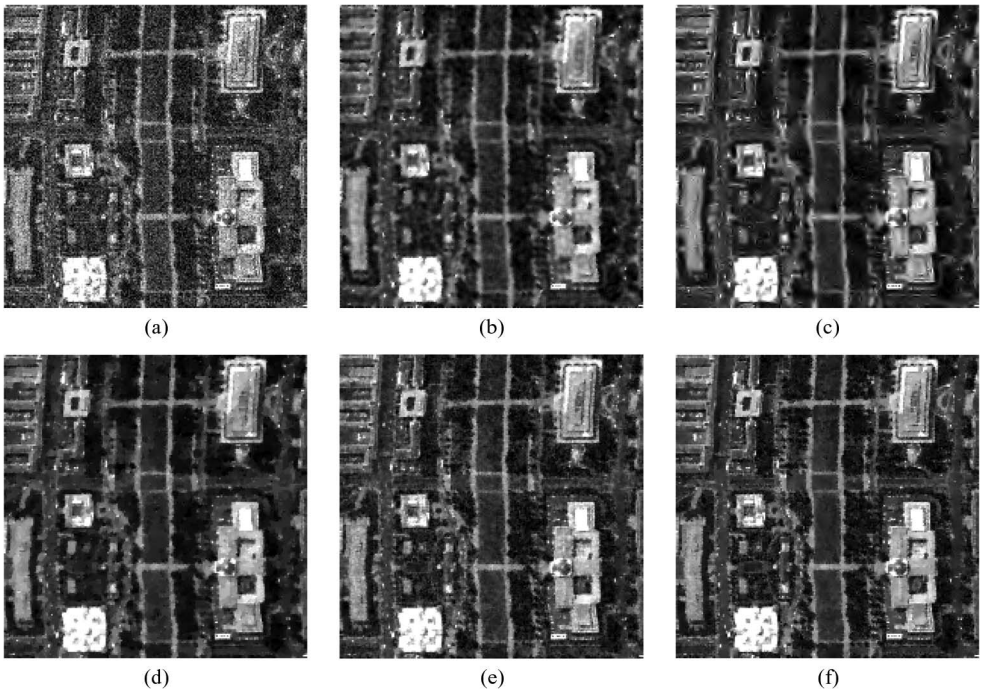

Fig. 7. Denoising results in simulated experiment Case 2. (a) Noise band 6, (b) locally adaptive Wiener, (c) wavelet hard thresholding, (d) band-by-band TV, (e) HTV, and (f) proposed SSAHTV.

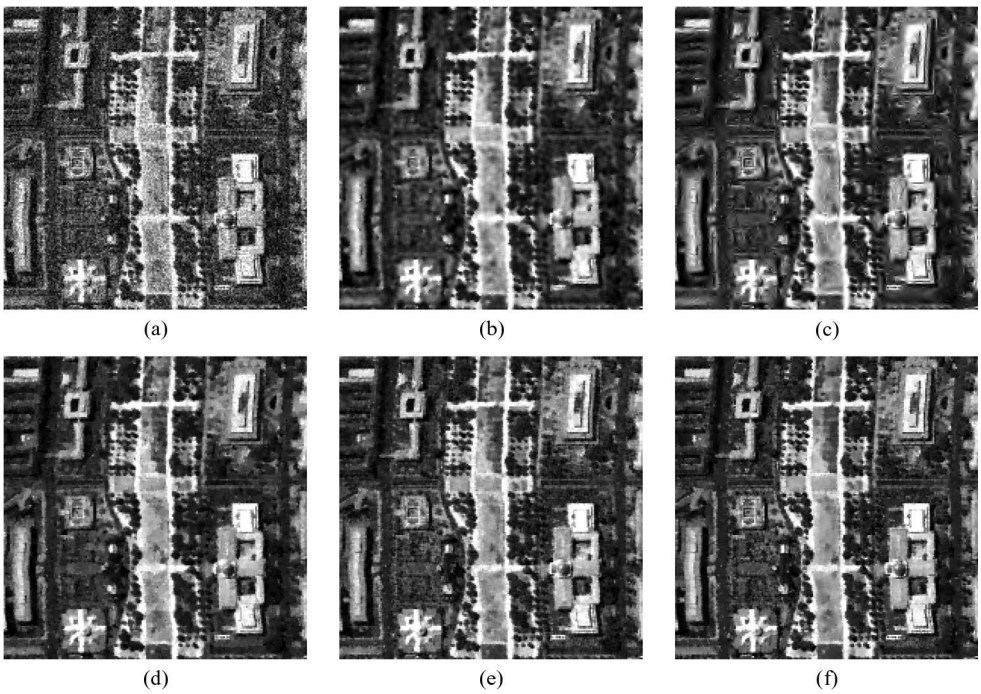

Fig. 8. Denoising results in simulated experiment Case 2. (a) Noise band 108, (b) locally adaptive Wiener, (c) wavelet hard thresholding, (d) band-by-band TV, (e) HTV, and (f) proposed SSAHTV.

the other four methods. In the overall quantitative assessment presented in Tables I and II, the proposed SSAHTV model has the highest MPSNR and MSSIM values of all the algorithms, which is consistent with the visual effect shown in Figs. 4 and 5 and Figs. 7 and 8.

It is shown from the simulated experimental results in Case 1 and Case 2 that the proposed SSAHTV method can provide a better and more robust denoising result, regardless of whether the noise intensity distributed in each band is equal or not, because of the spectral–spatial adaptive mechanism.

In Tables I and II, the computation times of the different algorithms are presented, from which it is shown that, of the four methods, the proposed SSAHTV denoising algorithm works very efficiently, and the computation time is only slightly longer than that of the simple locally adaptive Wiener filter, which

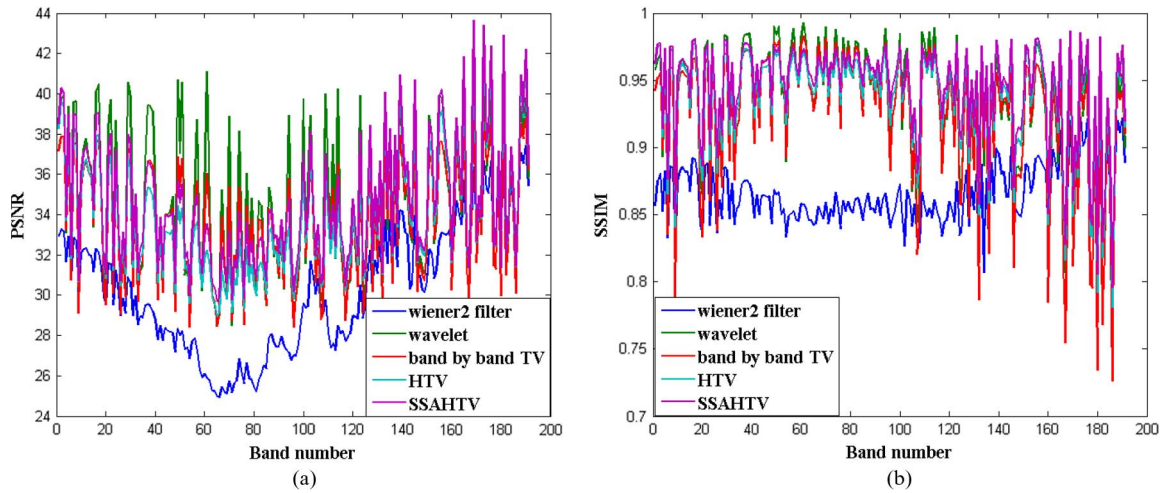

Fig. 9. PSNR and SSIM values of the different denoising approaches in each band of the simulated experiment Case 2. (a) PSNR value. (b) SSIM value.

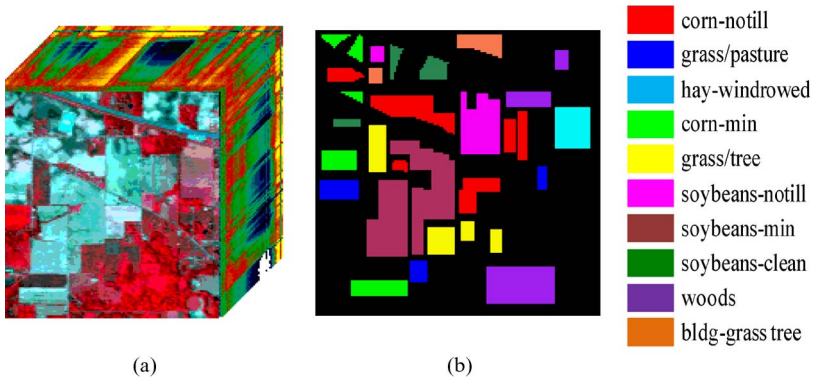

Fig. 10. AVIRIS Indian Pines data set used in the real data experiment 1. (a) Hyperspectral 3-D cube. (b) Training and test samples used in classification.

reflects the effectiveness of the split Bregman optimization algorithm.

B. Real Data Experiments

The AVIRIS Indian Pines test data shown in Fig. 10(a) were used in the first real data experiment. The data size is $145 * 145$ pixels, with 220 bands. It was provided by Professor David Landgrebe and can be downloaded from [40]. Before the denoising processing, the atmospheric and water absorption bands from bands 150–163 were removed from the original hyperspectral image. Therefore, there were only 206 bands used in the experiment.

The denoising results of three bands of the overall hyperspectral image are presented to give a comparison. The denoising results of bands 3, 110, and 204 are shown in Figs. 11–13, respectively. Fig. 14 shows the combination result of the three bands. From the denoising results, it can be clearly seen that the proposed SSAHTV model gives better denoising results than the other three methods. The denoising result using the locally adaptive Wiener filter appears oversmoothed, and most of the edge information is lost. In the wavelet hard thresholding denoising result, because the filter threshold in the wavelet domain is selected based on the whole image, ignoring the spatial information variation of the image, most of the detailed information is lost, and the denoising result is oversmoothed.

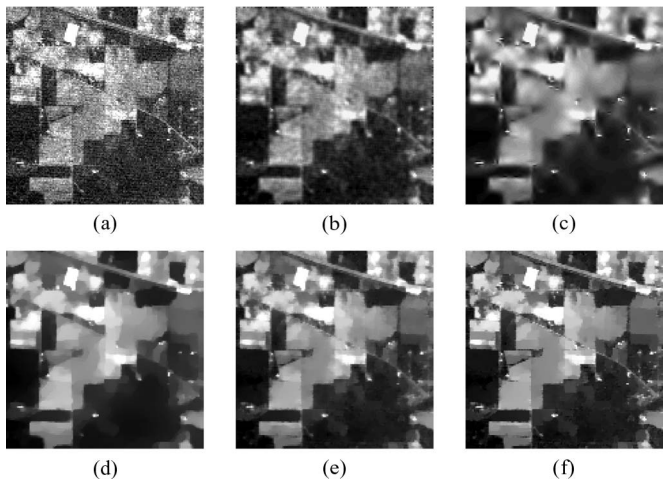

Fig. 11. Denoising results in the real data experiment 1. (a) Original noise band 3, (b) locally adaptive Wiener, (c) wavelet hard thresholding, (d) band-by-band TV, (e) HTV, and (f) proposed SSAHTV.

In the denoising results using the band-by-band TV model, because the noise intensity difference between different bands and the spatial information differences between different pixels are not considered, an equal denoising strength is used in all bands and all pixels; the denoising image is oversmoothed, and some detailed information, such as edges and texture, is lost. In the denoising results using the HTV model in (7), because

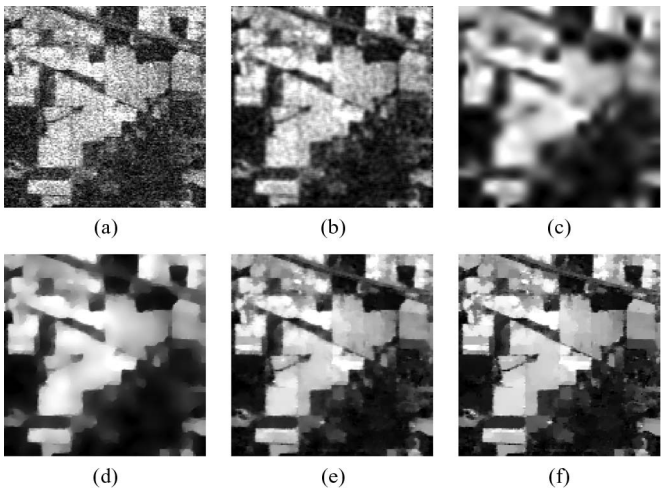

Fig. 12. Denoising results in the real data experiment 1. (a) Original noise band 110, (b) locally adaptive Wiener, (c) wavelet hard thresholding, (d) band-by-band TV, (e) HTV, and (f) proposed SSAHTV.

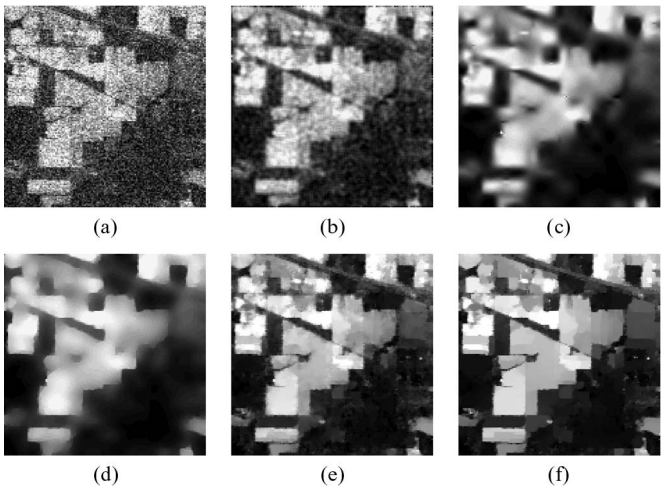

Fig. 13. Denoising results in the real data experiment 1. (a) Original noise band 204, (b) locally adaptive Wiener, (c) wavelet hard thresholding, (d) band-by-band TV, (e) HTV, and (f) proposed SSAHTV.

the spatial information difference between different pixels is not considered, the edge information appears a little blurred. However, in the denoising results of the proposed SSAHTV model, because the spectral and spatial adaptive processes are considered in the denoising and different denoising strengths are used in different bands and pixels, it is seen that the noise in the smooth area is sufficiently suppressed, while the edge information is well preserved. In particular, for the bands 110 and 204, because the signal in these two bands is so weak and the noise intensity appears so high, the denoising results using the band-by-band TV model appear so smooth that a majority of the edge and texture information is lost. However, in the denoising results using the proposed SSAHTV model, the edge information is well maintained, and the noise information is suppressed very well.

To further verify the effectiveness of the proposed denoising approach, the classification results of the hyperspectral image before and after denoising are given for comparison purposes. The training and test samples of the classification are shown

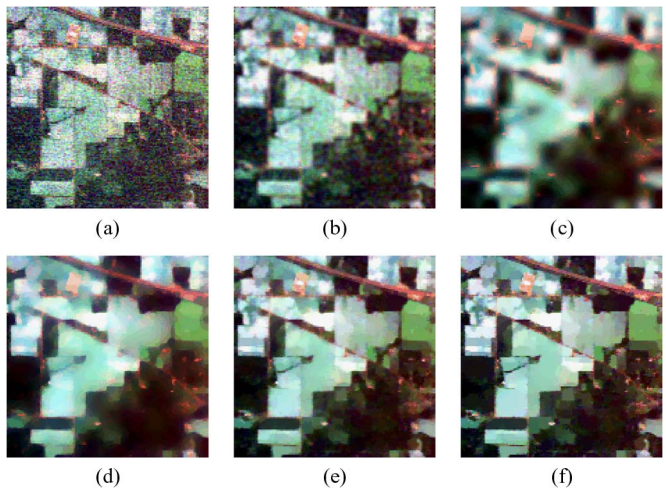

Fig. 14. Denoising results in the real data experiment 1. (a) Original band combination of the noise bands 3, 110, and 204, (b) locally adaptive Wiener, (c) wavelet hard thresholding, (d) band-by-band TV, (e) HTV, and (f) proposed SSAHTV.

TABLE III
NUMBER OF TRAINING AND TEST SAMPLES USED IN THE CLASSIFICATION OF THE AVIRIS INDIAN PINES DATA SET

Information classes	No. of training samples	No. of test samples
corn-notill	30	954
grass/pasture	30	296
hay-windrowed	30	327
corn-min	30	519
grass/tree	30	464
soybeans-notill	30	634
soybeans-min	30	1729
soybeans-clean	30	210
woods	30	882
bldg-grass tree	30	254

in Fig. 13(b), and the number of training and test samples is presented in Table III. To show that the classification improvement after image denoising is statistically significant, we first randomly select a few samples from the total samples as training samples, and we then use the support vector machine (SVM) classification method [47] to do a supervised classification for the image. Finally, the classification accuracy is tested with the remaining samples. The classification process is repeated ten times in our paper, and the mean overall accuracy (OA) and kappa coefficient are noted as the final classification assessment results. The classification results using SVM on the whole hyperspectral image are shown in Fig. 15(a)–(e). In Fig. 16(a)–(e), we also show the classification results using SVM after PCA, and the PC number in our experiment is selected to be ten. The classification accuracy evaluation results using OA and kappa coefficient are shown in Tables IV and V.

It is clearly seen that the classification result has been greatly improved after the denoising process. In the original noisy

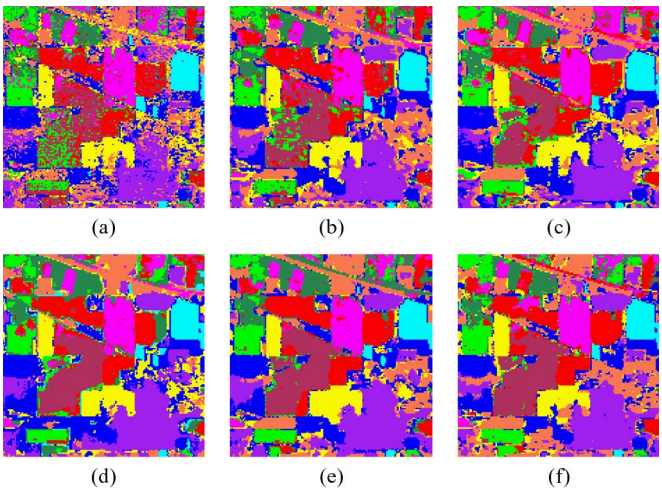

Fig. 15. Classification results using SVM before and after denoising of the real data experiment 1. (a) Classification result of the original image. (b) Classification result after locally adaptive Wiener denoising. (c) Classification result after wavelet hard thresholding denoising. (d) Classification result after band-by-band TV model denoising. (e) Classification result after HTV model denoising. (f) Classification result after proposed SSAHTV model denoising.

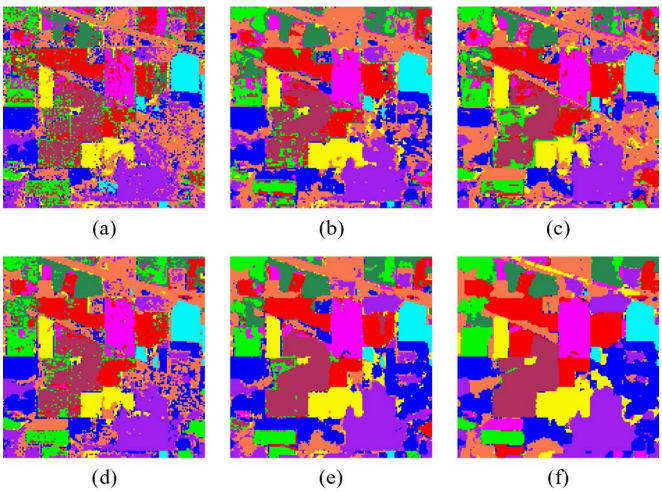

Fig. 16. Classification results using PCA+SVM before and after denoising in the real data experiment 1. (a) Classification result of the original image. (b) Classification result after locally adaptive Wiener denoising. (c) Classification result after wavelet hard thresholding denoising. (d) Classification result after band-by-band TV model denoising. (e) Classification result after HTV model denoising. (f) Classification result after proposed SSAHTV model denoising.

TABLE IV
SVM CLASSIFICATION ACCURACY EVALUATION RESULTS ON THE ORIGINAL IMAGE AFTER DENOISING OF THE REAL DATA EXPERIMENT 1

	Original image	Wiener	Wavelet	Band-by-band TV	HTV	SSAHTV
OA	77.01%	89.29%	91.40%	93.88%	93.69%	96.99%
Kappa	0.7341	0.8753	0.8996	0.9284	0.9262	0.9646

classification result, the classification appears fragmentary, because of the effect of the strong noise information in most of the bands, and the OA and kappa coefficient are only 77.01% and 0.7341 in the whole image classification result and 80.58% and 0.7750 in the classification result after PCA, respectively. However, in the denoised image classification result, the fragmentary effect is well reduced because the noise is suppressed. Of the four classification results from the different denoising methods, it is shown that the proposed approach gives the best classification result; it gives the highest OA and kappa coefficient values of 96.99% and 0.9646 in the whole image classification result and 97.40% and 0.9695 in the classification result after PCA, respectively.

TABLE V
PCA+SVM CLASSIFICATION ACCURACY EVALUATION RESULTS ON THE ORIGINAL IMAGE AFTER DENOISING OF THE REAL DATA EXPERIMENT 1

	Original image	Wiener	Wavelet	Band-by-band TV	HTV	SSAHTV
OA	80.58%	90.46%	88.08%	88.99%	96.69%	97.40%
Kappa	0.7750	0.8890	0.8609	0.8718	0.9612	0.9695

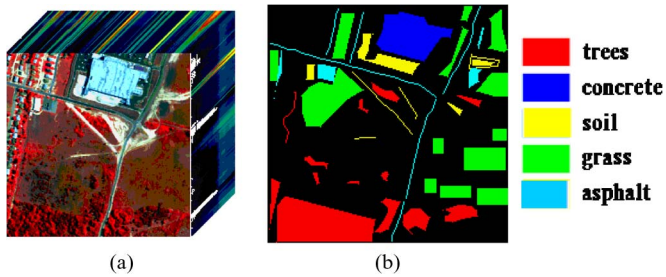

Fig. 17. HYDICE urban data sets used in the real data experiment 2. (a) Hyperspectral cube. (b) Training samples used in classification.

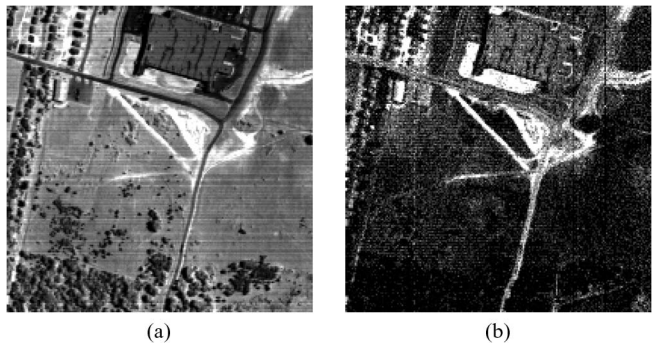

Fig. 18. Striping-noise and mixed-noise bands included in the HYDICE urban data sets in the real data experiment 2. (a) Striping-noise band. (b) Mixed-noise band (more than one type of noise).

The reason why the PCA-based classification result is improved after the process of denoising can be explained as follows. Because the PCA process ranked the PCs using the data variance, it is obvious that both signal and noise can contribute to data variance. Therefore, it is possible that some noise information may be included in the high-rank PCs, and this has a negative effect on the classification results. Consequently, with denoising processing before the PCA, because the noise information is suppressed, the classification result is improved. As the noise information is better suppressed with our proposed algorithm, a better classification result is produced.

In Table VI, to show the spectral fidelity, we also give some blind image quality assessment results using the mean spectral

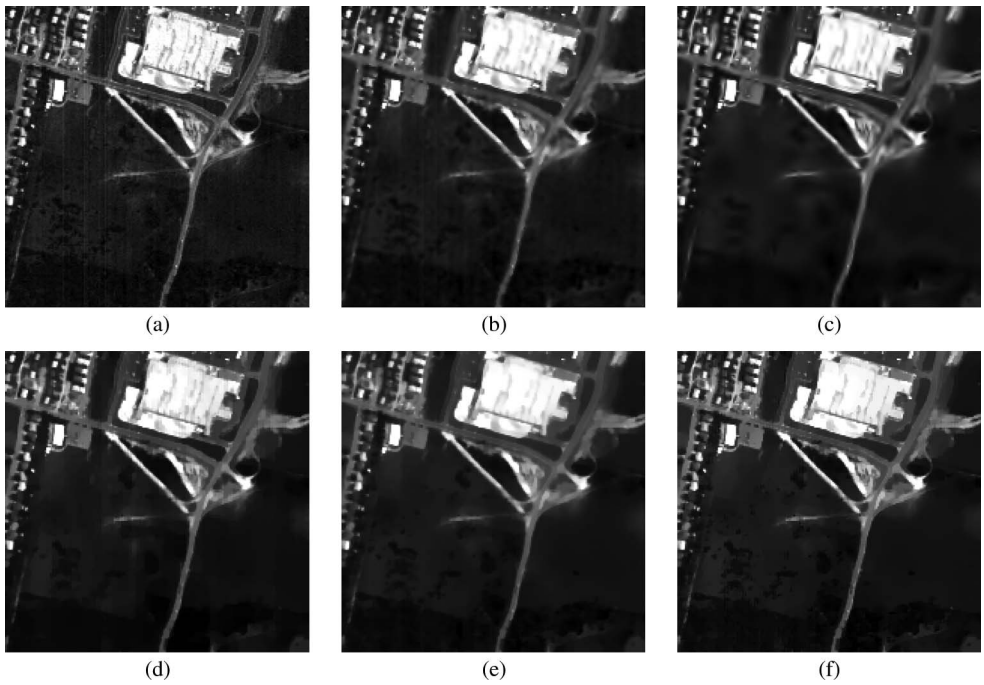

Fig. 19. Denoising results in the real data experiment 2. (a) Original noise band 2, (b) locally adaptive Wiener, (c) wavelet hard thresholding, (d) band-by-band TV, (e) HTV, and (f) proposed SSAHTV.

TABLE VI
BLIND QUALITY ASSESSMENT USING THE Q-METRIC IN REAL DATA EXPERIMENT 1

	Wiener	Wavelet	Band-by-band TV	HTV	SSAHTV
Q-mean	0.0519	0.0673	0.0635	0.0601	0.0646
SA-mean	0.8583	0.5446	0.8577	0.4926	0.4401
Time (s)	5.531	296.828	58.539	20.953	27.266

TABLE VII
NUMBER OF TRAINING SAMPLES USED IN THE CLASSIFICATION OF THE HYDICE URBAN DATA SETS

Information class	No. of training samples	No. of test samples
trees	30	3737
concrete	30	1584
soil	30	812
grass	30	4354
asphalt	30	742

angle (SA-mean) between the denoised image and the original noisy image. A recent blind image content measurement index called the Q-metric [48] is used to evaluate the spatial information preservation. In the same way as with the MPSNR and SSIM indices in the simulated experiment, we first compute the Q-metric value of each band, and the mean value of the Q-metric is set as the final evaluation result.

From the evaluation results using the mean spectral angle, it is shown that the proposed SSAHTV model produces the smallest mean spectral angle, which illustrates that the SSAHTV provides the smallest spectral distortion. In the spatial preserving evaluation result using the Q-metric, it is seen that although the wavelet hard thresholding method gives a slighter higher Q-metric value, we think that the excellent performance of the SSAHTV denoising method is sufficiently reflected in the visual and classification results mentioned earlier, and the proposed method also has a higher processing speed than the wavelet method and band-by-band TV model.

In the second real data experiment, the HYDICE urban image shown in Fig. 17 is used as the test data set. It is a size of 200 * 200 pixels and 205 bands. This experimental data set is available from [49]. We used this data set as there are considerable high-intensity striping- and mixed-noise (more than one type of noise) bands included in the data, examples of which are shown in Fig. 18. In Fig. 18(a), significant striping noise is included in the band, and a large amount of mixed noise is included in Fig. 19(b). Before the denoising processing, the atmospheric and water absorption bands from bands 140–151 have been removed from the original hyperspectral image. Therefore, there are only 193 bands used in the experiment. The training and test samples of the classification are shown in Fig. 17(b), and the numbers of the training and test samples are presented in Table VII.

Three bands of the hyperspectral image, bands 2, 103, and 193, are presented to illustrate the effectiveness of the proposed algorithm. The denoising results of these bands are shown in Figs. 19–21. The band combination result before and after denoising is shown in Fig. 22. The classification results using SVM for the whole hyperspectral image are shown in Fig. 23(a)–(e). Fig. 24(a)–(e) shows the SVM classification results after a PCA process on the hyperspectral image. The PC number is also selected to be ten. The classification accuracy and quantitative evaluation results are shown in Tables VIII–X.

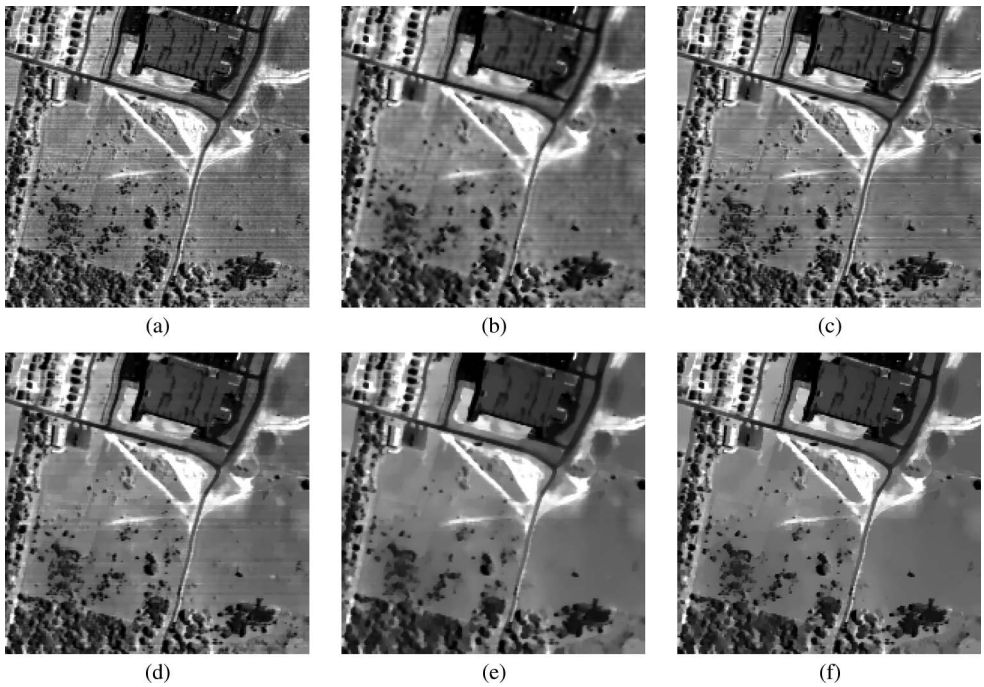

Fig. 20. Denoising results in the real data experiment 2. (a) Original noise band 103, (b) locally adaptive Wiener (c), wavelet hard thresholding, (d) band-by-band TV, (e) HTV, and (f) proposed SSAHTV.

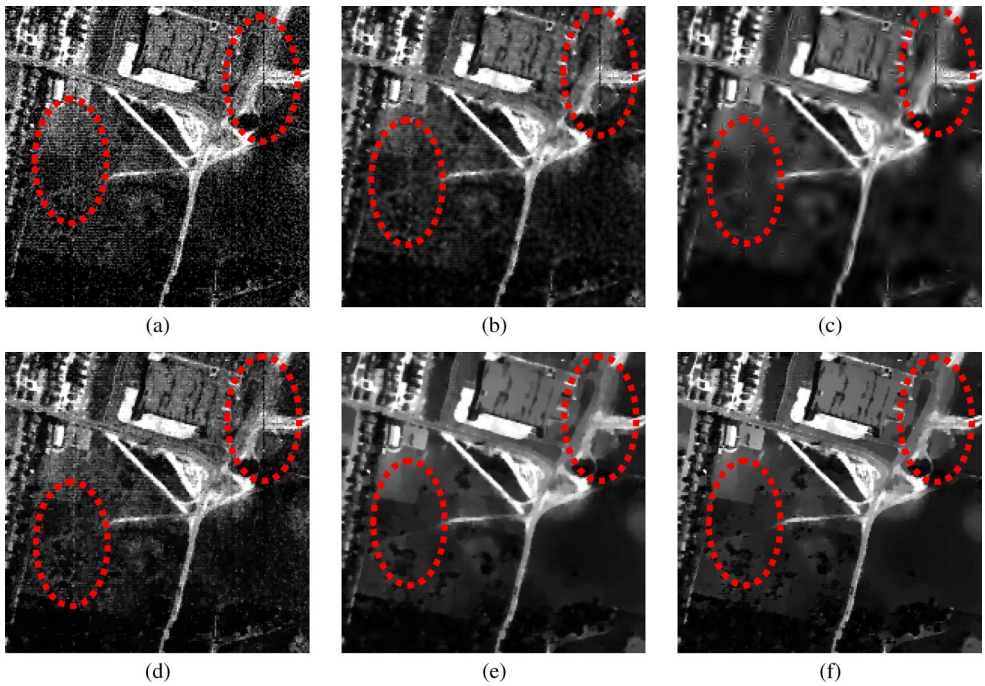

Fig. 21. Denoising results in the real data experiment 2. (a) Original noise band 193, (b) locally adaptive Wiener (c), wavelet hard thresholding, (d) band-by-band TV, (e) HTV, and (f) proposed SSAHTV.

From the denoising results shown in Figs. 19–22, it can be clearly seen that the proposed SSAHTV denoising approach performs better and provides a better striping- and mixed-noise removing effect than the other three methods. In Figs. 19(e) and 20(e), the striping noise that exists in the original image shown in Figs. 19(a) and 20(a) is better suppressed, without losing the edge and detailed information. For the mixed noise shown in Fig. 21(a), the proposed approach also produces promising results. In Fig. 21(e), it can be clearly seen that almost all the noise is removed completely, without losing the edge information. However, for the other four denoising results, the striping noise is not well removed, either the denoising result is over smooth or the striping noise is not completely removed. It should be noted in Fig. 21 that a dead pixel line existed in the original image. With the proposed SSAHTV method, the dead pixel line can be easily removed. From the aforementioned observations, we think that the proposed model may well provide

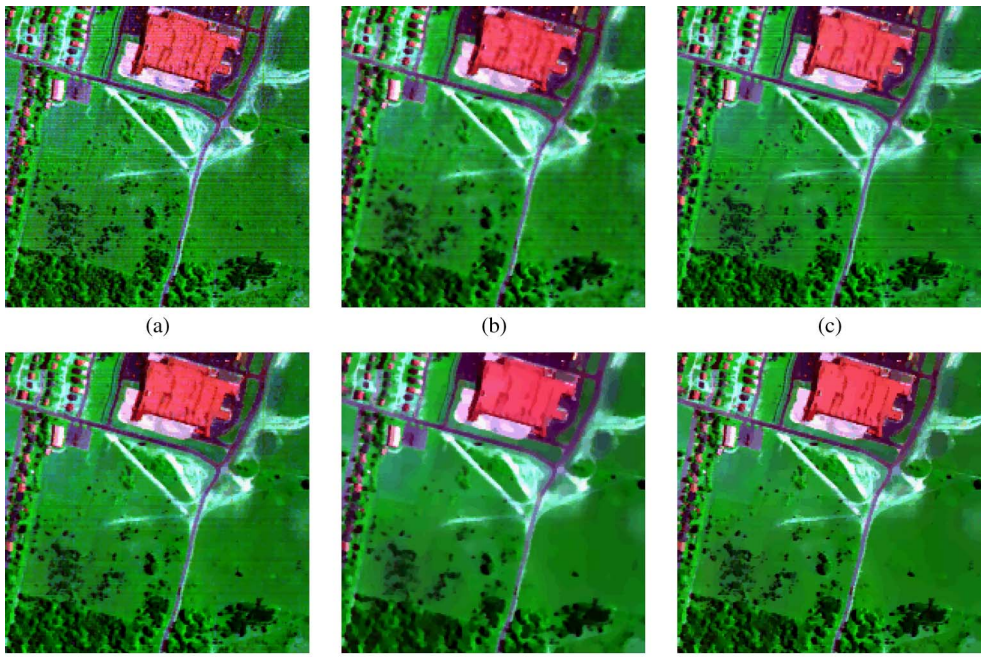

Fig. 22. Denoising results in the real data experiment 2. (a) Original band combination of the noise bands 2, 103, and 192, (b) combination after locally adaptive Wiener, (c) combination after wavelet hard thresholding, (d) combination after band-by-band TV, (e) combination after HTV, and (f) combination after proposed SSAHTV.

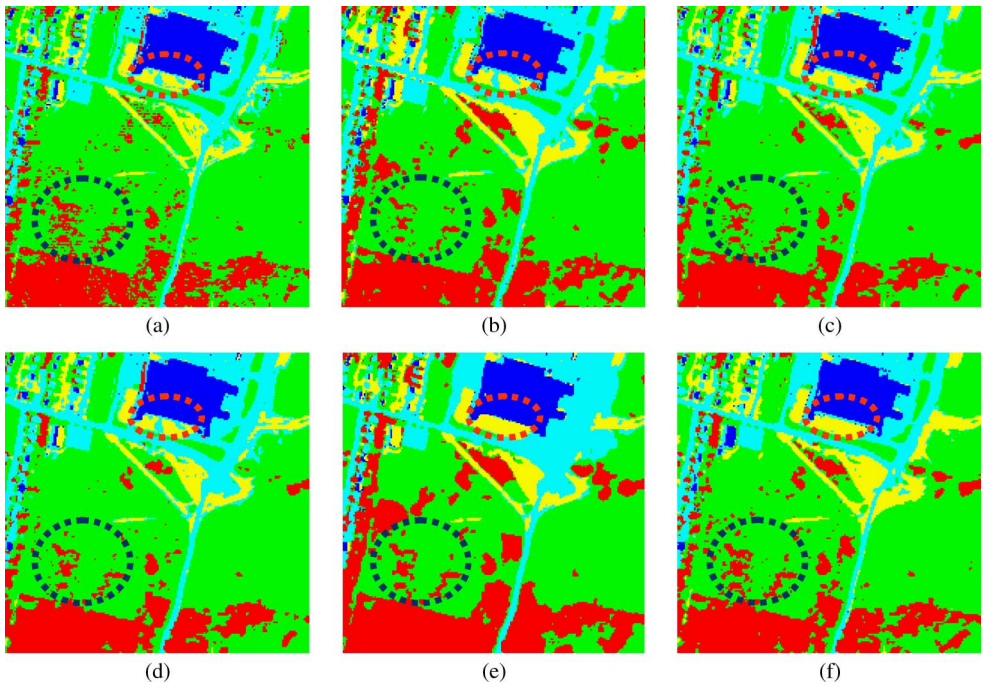

Fig. 23. Classification results using SVM before and after denoising of the real experiment 2. (a) Classification result of the original image. (b) Classification result after locally adaptive Wiener denoising. (c) Classification result after wavelet hard thresholding denoising. (d) Classification result after band-by-band TV model denoising. (e) Classification result after HTV model denoising. (f) Classification result after proposed SSAHTV model denoising.

a new idea for hyperspectral image destriping and dead pixel inpainting.

The classification results shown in Figs. 23 and 24 also reflect the effectiveness of the proposed approach. In these two figures, the proposed SSAHTV model denoised image produces a better classification image, which is reflected in the OA and kappa coefficient presented in Tables VIII and IX.

C. Discussion

1) Sensitivity Analysis of the Parameter μ: In (14), to define the spatially weighted parameter of each pixel in the denoising process, we use the parameter u to control the contribution of the spatial information on the spatial weight τ_i. To show its effect on the final denoising performance, using simulated

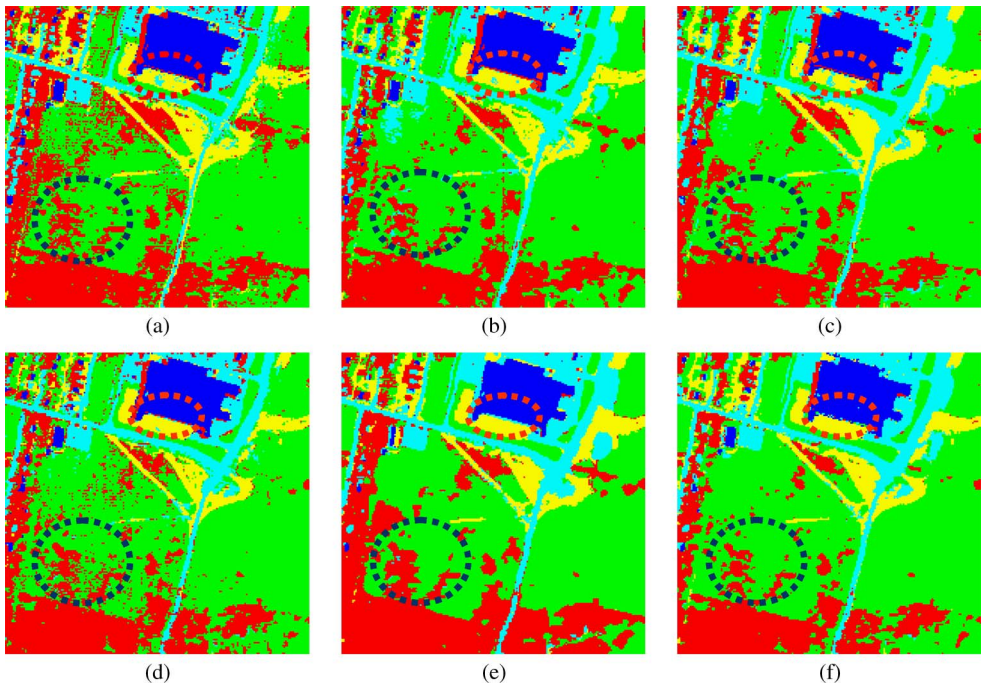

Fig. 24. Classification results using PCA+SVM before and after denoising in the real data experiment 2. (a) Classification result of the original image. (b) Classification result after locally adaptive Wiener denoising. (c) Classification result after wavelet hard thresholding denoising. (d) Classification result after band-by-band TV model denoising. (e) Classification result after proposed HTV model denoising. (f) Classification result after proposed SSAHTV model denoising.

TABLE VIII
SVM CLASSIFICATION ACCURACY EVALUATION RESULTS ON THE ORIGINAL IMAGE AFTER DENOISING OF THE REAL DATA EXPERIMENT 2

	Original image	Wiener	Wavelet	Band-by-band TV	HTV	SSAHTV
OA	92.06%	92.36%	92.52%	92.69%	95.75%	96.80%
Kappa	0.8880	0.9063	0.8943	0.8968	0.9409	0.9554

TABLE IX
PCA+SVM CLASSIFICATION ACCURACY EVALUATION RESULTS ON THE ORIGINAL IMAGE AFTER DENOISING OF THE REAL DATA EXPERIMENT 2

	Original image	Wiener	Wavelet	Band-by-band TV	HTV	SSAHTV
OA	93.21%	93.64%	94.40%	93.29%	96.69%	95.07%
Kappa	0.9045	0.9111	0.9213	0.9051	0.9570	0.9305

TABLE X
BLIND QUALITY ASSESSMENT USING THE Q-METRIC IN REAL DATA EXPERIMENT 2

	Wiener	Wavelet	Band-by-band TV	HTV	SSAHTV
Q-mean	0.1435	0.1648	0.1545	0.1350	0.1557
SA-mean	4.4715	3.5017	3.7601	3.5011	3.2056
Time (s)	6.688	539.36	213.906	86.203	48.281

experiment Case 1 as an example, we give a sensitivity analysis for this parameter, which is shown in Figs. 25 and 26.

Fig. 25 shows the change of the MPSNR and MSSIM values with the change of the parameter μ from 1 to 200, and Fig. 26 shows the change of the PSNR and SSIM values for different bands when the parameter μ is respectively set with a small value (10) and a large value (200).

From these figures, it is shown that the denoising results maintain robustness with changes in parameter μ. In Fig. 25, the MPSNR and MSSIM values show little change with the change of parameter μ from 1 to 200. In Fig. 26(a) and (b), the PSNR and SSIM change curves with a small μ and large μ are almost overlapped, and the difference between them is close to zero [Fig. 26(c) and (d)], which sufficiently illustrates the robustness of the denoising result with the parameter μ.

The reason why the denoising result can maintain robustness with changes of this parameter can be explained as follows: In our paper, we first define a parameter τ_i with the spatial gradient information in (14), and then, the spatially weighted parameter W_i is defined in (15). From the definition, it is shown that, although the change parameter μ impacts the parameter τ_i, after the processing in (15), for the spatially weighted parameter W_i, the impact is much reduced and limited. For example, for (15), if the parameter τ_i becomes small with the change of μ, the mean value $\overline{\tau}$ of τ_i also becomes small; this arrangement ensures that parameter W_i shows little change, particularly when the parameter μG_i is larger than one.

2) Noise Robustness and Computation Time Analysis: To show the noise robustness of the proposed method, in Fig. 27, using simulated experiment 1 as an example, the performance changes of the different denoising methods with different SNR values are presented. From the figures, it is clearly shown that the proposed SSAHTV model maintains robustness and always performs better than the other methods with changes in noise intensity.

For the computation time, it is seen from Fig. 27(c) that the computation time of the proposed algorithm increases as

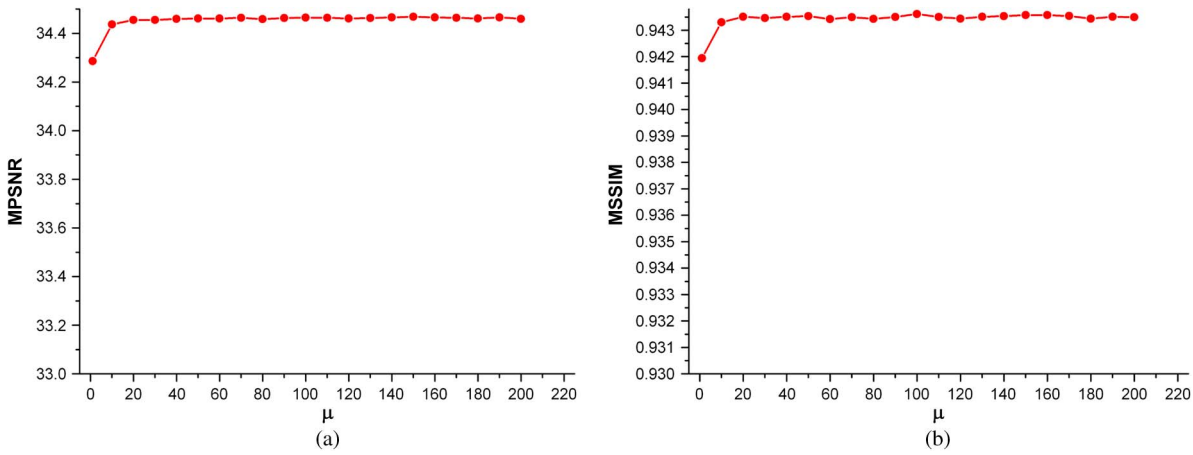

Fig. 25. Sensitivity analysis of parameter μ (μ from 1 to 200). (a) Change of the MPSNR value with the parameter μ. (b) Change of the MSSIM value with the parameter μ.

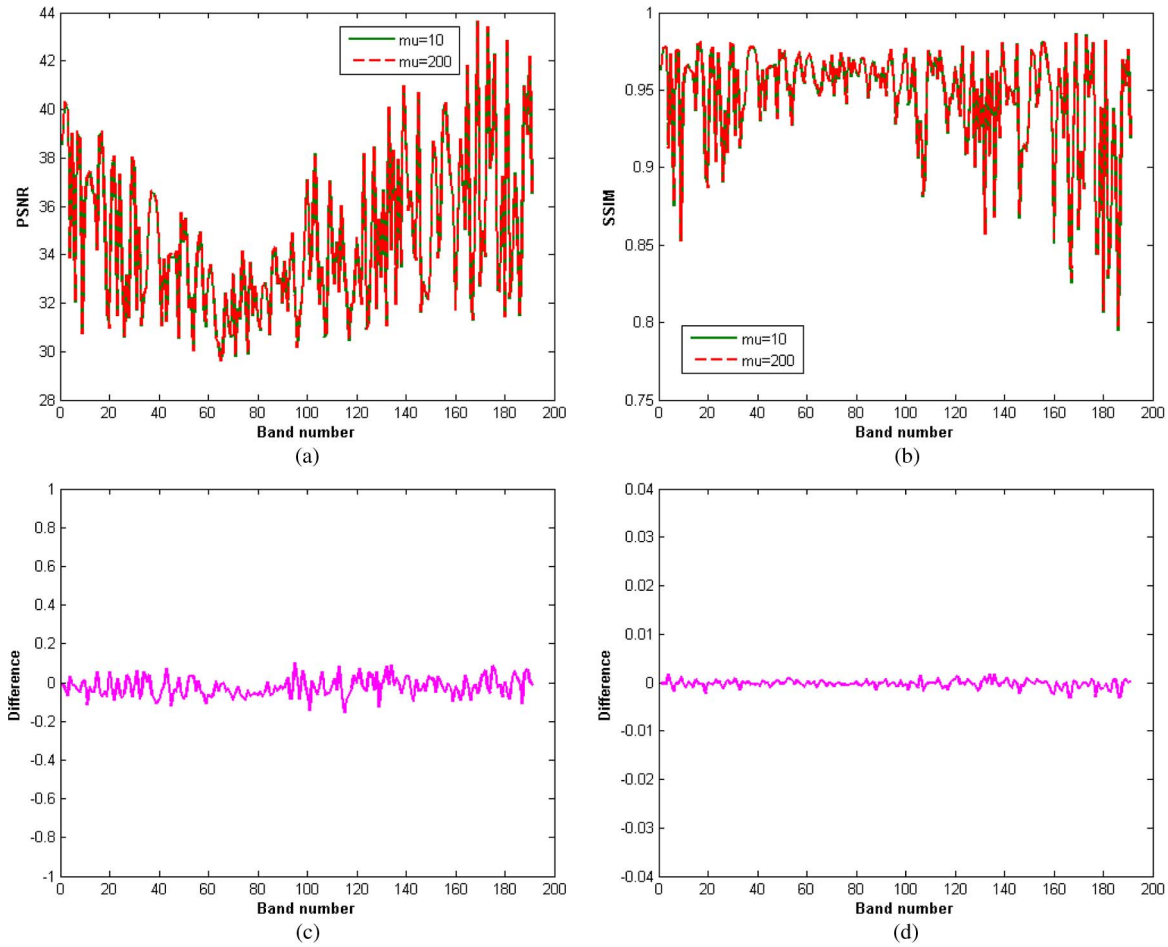

Fig. 26 Comparison of the PSNR and SSIM values in different bands with a small and large μ value ($\mu = 10$ and $\mu = 200$). (a) and (b) PSNR and SSIM value comparison. (c) and (d) PSNR and SSIM value difference of different bands with a small and large μ value.

noise intensity increases. In low-intensity conditions, it has a longer computation time than the simple locally adaptive Wiener filter. As the SNR value increases, the computation time also increases, and is close to the time of the wavelet denoising method and band-by-band TV denoising method, because the optimal iteration time is increasing. Although it may need a little longer computation time in high-noise-intensity conditions, the denoising effect of the proposed method is the best of all four algorithms.

VI. Conclusion

In this paper, we have proposed a spectral–spatial adaptive TV hyperspectral image denoising algorithm, in which the

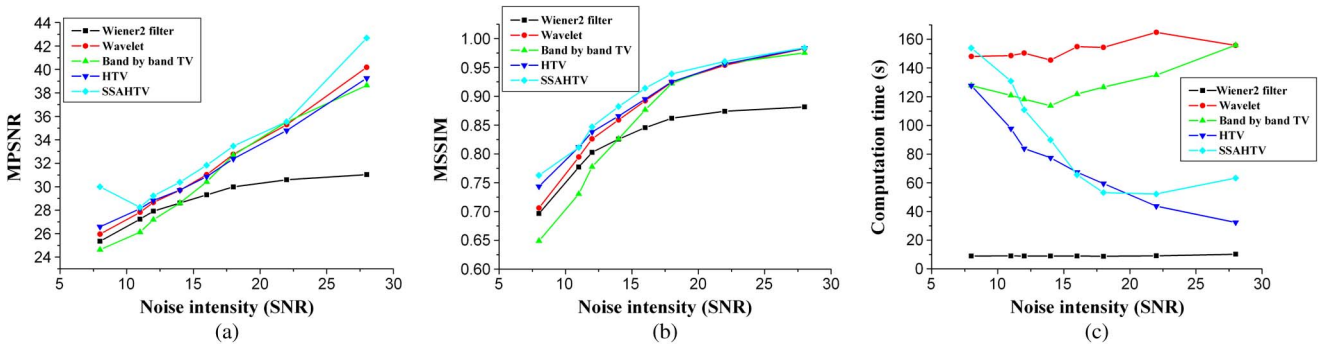

Fig. 27 Change of the denoising result of different denoising algorithms with different noise level (SNR). (a) PSNR value change. (b) MSSIM value change. (c) Computation time change.

noise distribution difference between different bands and the spatial information difference between different pixels are both considered in the process of denoising. First, a MAP-based hyperspectral denoising model is constructed, which consists of two items: the data fidelity item and the regularization item. Then, for the regularization item, an SSAHTV model is proposed, which can control the denoising strength between different bands and pixels with different spatial properties. In different bands, a large denoising strength is enforced in a band with high noise intensity, and conversely, a small denoising strength is used in bands with low-intensity noise. At the same time, in different spatial property regions in the hyperspectral image, a large denoising strength is used in smooth areas to completely suppress noise, and a small denoising strength is used in the edge areas to preserve detailed information. Finally, the split Bergman iteration algorithm is used to optimize the spectral–spatial adaptive TV hyperspectral image denoising model in order to reduce the high computation load in the process of hyperspectral image denoising. Several simulated and real data sets were employed in experiments presented in Section V to illustrate that the proposed algorithm can satisfactorily balance the denoising strength in different hyperspectral bands and different spatial pixel locations, and produce a denoising result with noise well suppressed, but without loss of edge and detailed information. It is important to emphasize that the proposed approach also works well on high-intensity striping- and mixed-noise images, and it may well provide a new idea for hyperspectral image destriping and dead pixel inpainting.

Although the proposed SSAHTV model works well on the hyperspectral image denoising problem, it can still be further improved in some aspects. Our future work will focus on also considering the gradient in the spectral dimension in the model construction process in order to develop a real 3-D TV model. In addition, it may be possible to use the 3-D segmentation or clustering result to constrain the denoising process from a region perspective, rather than the pixel perspective in the present paper.

ACKNOWLEDGMENT

The authors would like to thank Prof. D. Landgrebe at Purdue University for providing the free downloads of the HYDICE image of Washington DC Mall and the AVIRIS Indian Pines test data. The authors would also like to thank the handling editor and anonymous reviewers for their careful reading and helpful remarks.

REFERENCES

[1] L. Zhang and X. Huang, "Object-oriented subspace analysis for airborne hyperspectral remote sensing imagery," *Neurocomputing*, vol. 73, no. 4–6, pp. 927–936, Jan. 2010.

[2] Y. Zhong, L. Zhang, B. Huang, and P. Li, "An unsupervised artificial immune classifier for multi/hyperspectral remote sensing imagery," *IEEE Trans. Geosci. Remote Sens.*, vol. 44, no. 2, pp. 420–431, Feb. 2006.

[3] H. Li and L. Zhang, "A hybrid automatic endmember extraction algorithm based on a local window," *IEEE Trans. Geosci. Remote Sens.*, vol. 49, no. 11, pp. 4223–4238, Nov. 2011.

[4] L. Zhang, K. Wu, Y. Zhong, and P. Li, "A new sub-pixel mapping algorithm based on a BP neural network with an observation model," *Neurocomputing*, vol. 71, no. 10–12, pp. 2046–2054, Jun. 2008.

[5] L. Zhang, B. Du, and Y. Zhong, "Hybrid detectors based on selective endmembers," *IEEE Trans. Geosci. Remote Sens.*, vol. 48, no. 6, pp. 2633–2646, Jun. 2010.

[6] I. Atkinson, F. Kamalabadi, and D. L. Jones, "Wavelet-based hyperspectral image estimation," in *Proc. IGARSS*, Toulouse, France, Jul. 2003, vol. 2, pp. 743–745.

[7] H. Othman and S. Qian, "Noise reduction of hyperspectral imagery using hybrid spatial-spectral derivative-domain wavelet shrinkage," *IEEE Trans. Geosci. Remote Sens.*, vol. 44, no. 2, pp. 397–408, Feb. 2006.

[8] G. Chen and S. Qian, "Simultaneous dimensionality reduction and denoising of hyperspectral imagery using bivariate wavelet shrinking and principal component analysis," *Can. J. Remote Sens.*, vol. 34, no. 5, pp. 447–454, Oct. 2008.

[9] G. Chen and S. Qian, "Denoising and dimensionality reduction of hyperspectral imagery using wavelet packets, neighbour shrinking and principal component analysis," *Int. J. Remote Sens.*, vol. 30, no. 18, pp. 4889–4895, Sep. 2009.

[10] S. Qian and J. Lévesque, "Target detection from noise-reduced hyperspectral imagery using a spectral unmixing approach," *Opt. Eng.*, vol. 48, no. 2, pp. 026401-1–026401-11, Feb. 2009.

[11] G. Chen, S. Qian, and W. Xie, "Denoising of hyperspectral imagery using principal component analysis and wavelet shrinkage," *IEEE Trans. Geosci. Remote Sens.*, vol. 49, no. 3, pp. 973–980, Mar. 2011.

[12] D. Letexier and S. Bourennane, "Noise removal from hyperspectral images by multidimensional filtering," *IEEE Trans. Geosci. Remote Sens.*, vol. 46, no. 7, pp. 2061–2069, Jul. 2008.

[13] N. Renard and S. Bourennane, "Improvement of target detection methods by multiway filtering," *IEEE Trans. Geosci. Remote Sens.*, vol. 46, no. 8, pp. 2407–2417, Aug. 2008.

[14] S. Bourennane, C. Fossati, and A. Cailly, "Improvement of classification for hyperspectral images based on tensor modeling," *IEEE Geosci. Remote Sens. Lett.*, vol. 7, no. 4, pp. 801–805, Oct. 2010.

[15] Y. Wang and R. Niu, "Hyperspectral urban remote sensing image smoothing and enhancement using forward-and-backward diffusion," presented at the Urban Remote Sensing Joint Event, Shanghai, China, May, 2009.

[16] Y. Wang, R. Niu, and X. Yu, "Anisotropic diffusion for hyperspectral imagery enhancement," *IEEE Sensors J.*, vol. 10, no. 3, pp. 469–477, Mar. 2010.

[17] J. M. Duarte-Carvajalino, P. E. Castillo, and M. Velez-Reyes, "Comparative study of semi-implicit schemes for nonlinear diffusion in

hyperspectral imagery," *IEEE Trans. Image Process.*, vol. 16, no. 5, pp. 1303–1314, May 2007.
[18] X. Huang and L. Zhang, "An adaptive mean-shift analysis approach for object extraction and classification from urban hyperspectral imagery," *IEEE Trans. Geosci. Remote Sens.*, vol. 46, no. 12, pp. 4173–4185, Dec. 2008.
[19] L. Rudin, S. Osher, and E. Fatemi, "Nonlinear total variation based noise removal algorithms," *Physica D*, vol. 60, no. 1–4, pp. 259–268, Nov. 1992.
[20] M. K. Ng, H. Shen, E. Y. Lam, and L. Zhang, "A total variation regularization based super-resolution reconstruction algorithm for digital video," *EURASIP J. Adv. Signal Process.*, vol. 2007, p. 74 585, 2007.
[21] M. Donoser, M. Urschler, M. Hirzer, and H. Bischof, "Saliency driven total variation segmentation," in *Proc. Int. Conf. Computer Vision*, Kyoto, Japan, Sep. 2009, pp. 817–824.
[22] A. Buades, T. M. Le, J. M. Morel, and L. A. Vese, "Fast cartoon + texture image filters," *IEEE Trans. Image Process.*, vol. 19, no. 8, pp. 1978–1986, Aug. 2010.
[23] P. Blomgren and T. F. Chan, "Color TV: Total variation methods for restoration of vector-valued images," *IEEE Trans. Image Process.*, vol. 7, no. 3, pp. 304–309, Mar. 1998.
[24] L. Bar, A. Brook, N. Sochen, and N. Kiryati, "Deblurring of color images corrupted by impulsive noise," *IEEE Trans. Image Process.*, vol. 16, no. 4, pp. 1101–1111, Apr. 2007.
[25] Y. Wen, M. K. Ng, and Y. Huang, "Efficient total variation minimization methods for color image restoration," *IEEE Trans. Image Process.*, vol. 17, no. 11, pp. 2081–2088, Nov. 2008.
[26] M. Jung, X. Bresson, T. F. Chan, and L. A. Vese, "Nonlocal Mumford-Shah regularizers for color image restoration," *IEEE Trans. Image Process.*, vol. 20, no. 6, pp. 1583–1598, Jun. 2011.
[27] X. Bresson and T. F. Chan, "Fast dual minimization of the vectorial total variation norm and applications to color image processing," *Inverse Probl. Imag.*, vol. 2, no. 4, pp. 455–484, Nov. 2008.
[28] C. Brito-Loeza and K. Chen, "On high-order denoising models and fast algorithms for vector-valued images," *IEEE Trans. Image Process.*, vol. 19, no. 6, pp. 1518–1527, Jun. 2010.
[29] D. M. Strong, P. Blomgren, and T. F. Chan, "Spatially adaptive local feature driven total variation minimizing image restoration," in *Proc. Conf. Stat. Stochastic Methods Image Process. II*, F. Preteux, J. L. Davidson, and E. R. Dougherty, Eds., San Diego, CA, 1997, pp. 222–233.
[30] G. Gilboa, N. Sochen, and Y. Y. Zeevi, "PDE-based denoising of complex scenes using a spatially-varying fidelity term," in *Proc. Int. Conf. Image Process.*, Barcelona, Spain, 2003, pp. I-865–I- 868.
[31] A. Chopra and H. Lian, "Total variation, adaptive total variation and nonconvex smoothly clipped absolute deviation penalty for denoising blocky images," *Pattern Recognit.*, vol. 43, no. 8, pp. 2609–2619, Aug. 2010.
[32] X. Li, Y. Hu, and X. B. Gao, "A multi-frame image super resolution method," *Signal Process.*, vol. 90, no. 2, pp. 405–414, Feb. 2010.
[33] A. B. Hamza and H. Krim, "A variational approach to maximum a posteriori estimation for image denoising," in *Proc. EMMCVPR*, vol. 2134, *Lecture Notes in Computer Science*, Sep. 2001, pp. 19–33.
[34] H. Shen and L. Zhang, "A MAP-based algorithm for destriping and inpainting of remotely sensed images," *IEEE Trans. Geosci. Remote Sens.*, vol. 47, no. 5, pp. 1492–1502, May 2009.
[35] H. Shen, L. Zhang, B. Huang, and P. Li, "A MAP approach for joint motion estimation, segmentation, and super resolution," *IEEE Trans. Image Process.*, vol. 16, no. 2, pp. 479–490, Feb. 2007.
[36] Q. Yuan, L. Zhang, H. Shen, and P. Li, "Adaptive multiple-frame image super-resolution based on U-curve," *IEEE Trans. Image Process.*, vol. 19, no. 12, pp. 3157–3170, Dec. 2010.
[37] L. Bregman, "The relaxation method of finding the common points of convex sets and its application to the solution of problems in convex optimization," *USSR Comp. Math. Math.*, vol. 7, pp. 200–217, 1967.
[38] T. Goldstein and S. Osher, "The split bregman method for L1 regularized problems," *SIAM J. Imag. Sci.*, vol. 2, no. 2, pp. 323–343, May 2009.
[39] D. L. Donoho, "De-noising by soft-thresholding," *IEEE Trans. Inf. Theory*, vol. 41, no. 3, pp. 613–627, May 1995.
[40] [Online]. Available: https://engineering.purdue.edu/~biehl/MultiSpec/hyperspectral.html
[41] [Online]. Available: http://www.mathworks.cn/help/toolbox/images/ref/wiener2.html
[42] Toolbox Wavelets—A Toolbox for Multiscale Signal and Image Processing. [Online]. Available: http://www.ceremade.dauphine.fr/~peyre/matlab/wavelets/content.html
[43] Z. Wang, A. C. Bovik, and H. R. Sheikh, "Image quality assessment: From error visibility to structural similarity," *IEEE Trans. Image Process.*, vol. 13, no. 4, pp. 600–612, Apr. 2004.
[44] Z. Wang and A. C. Bovik, "Mean squared error: Love it or leave it?—A new look at signal fidelity measures," *IEEE Signal Process. Mag.*, vol. 26, no. 1, pp. 98–117, Jan. 2009.
[45] X. Gao, W. Lu, D. Tao, and X. Li, "Image quality assessment based on multiscale geometric analysis," *IEEE Trans. Image Process.*, vol. 18, no. 7, pp. 1409–1423, Jul. 2009.
[46] D. Tao, X. Li, W. Lu, and X. Gao, "Reduced-reference IQA in contourlet domain," *IEEE Trans. Syst., Man, Cybern. B, Cybern.*, vol. 39, no. 6, pp. 1623–1627, Dec. 2009.
[47] L. Zhang, L. Zhang, D. Tao, and X. Huang, "On combining multiple features for hyperspectral remote sensing image classification," *IEEE Trans. Geosci. Remote Sens.*, vol. 50, no. 3, pp. 879–893, Mar. 2012.
[48] X. Zhu and P. Milanfar, "Automatic parameter selection for denoising algorithms using a no-reference measure of image content," *IEEE Trans. Image Process.*, vol. 19, no. 12, pp. 3116–3112, Dec. 2010.
[49] [Online]. Available: http://www.tec.army.mil/hypercube

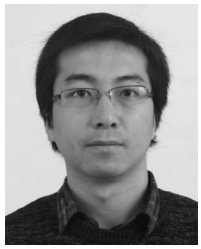

Qiangqiang Yuan received the B.S. degree in surveying and mapping engineering from Wuhan University, Wuhan, China, in 2006, where he is currently working toward the Ph.D. degree in the State Key Laboratory of Information Engineering in Surveying, Mapping, and Remote Sensing.

His current research interests focus on image restoration, superresolution, and remote sensing image enhancement.

Liangpei Zhang (M'06–SM'08) received the B.S. degree in physics from Hunan Normal University, ChangSha, China, in 1982, the M.S. degree in optics from the Xi'an Institute of Optics and Precision Mechanics of the Chinese Academy of Sciences, Xi'an, China, in 1988, and the Ph.D. degree in photogrammetry and remote sensing from Wuhan University, Wuhan, China, in 1998.

He is currently with the State Key Laboratory of Information Engineering in Surveying, Mapping, and Remote Sensing, Wuhan University, as the Head of the Remote Sensing Division. He is also currently a "Chang-Jiang Scholar" Chair Professor appointed by the Ministry of Education, China. He is currently a Principal Scientist for the China State Key Basic Research Project (2011–2016) appointed by the Ministry of National Science and Technology of China to lead the remote sensing program in China. He has more than 200 research papers and is the holder of five patents. His research interests include hyperspectral remote sensing, high-resolution remote sensing, image processing, and artificial intelligence.

Dr. Zhang is a Fellow of the IEE, an executive member (Board of Governor) of the China National Committee of International Geosphere–Biosphere Programme, an executive member for the China Society of Image and Graphics, and others. He regularly serves as a Cochair of the series SPIE Conferences on Multispectral Image Processing and Pattern Recognition (MIPPR), Conference on Asia Remote Sensing, and many other conferences. He edits several conference proceedings, issues, and the Geoinformatics Symposiums. He also serves as an Associate Editor of the *International Journal of Ambient Computing and Intelligence*, *International Journal of Image and Graphics*, *International Journal of Digital Multimedia Broadcasting*, *Journal of Geospatial Information Science*, and *Journal of Remote Sensing*.

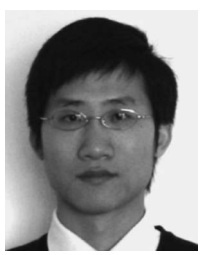

Huanfeng Shen (M'11) received the B.S. degree in surveying and mapping engineering and the Ph.D. degree in photogrammetry and remote sensing from Wuhan University, Wuhan, China, in 2002 and 2007, respectively.

Since July 2007, he has been with the School of Resource and Environmental Science, Wuhan University, where he is currently an Associate Professor. His research interests focus on image reconstruction, remote sensing, image processing and application, and data fusion and assimilation.